Contents

S1 L-curve-based adaptive regularization strategy

The regularization factor controls the balance between the background constraint and the observational constraint in the 4D-Var cost function. A small regularization factor allows larger emission adjustments and can improve the fit to observations, but may also amplify noise or generate unstable posterior corrections. A large regularization factor keeps the posterior emissions close to the a priori inventory, but may leave substantial observation residuals. The L-curve provides a diagnostic way to select this balance by plotting the norm of the regularized solution, or equivalently the background penalty, against the norm of the residual, or the observation mismatch, for a set of candidate regularization factors. The preferred value is located near the corner of the L-curve, where further reduction in observation mismatch would require a disproportionately large departure from the prior state.

In CoMIAR v1.0, the L-curve criterion was used in an online iterative manner rather than as a one-time offline tuning step. During the 4D-Var optimization, the background penalty and observation mismatch were recalculated as the inversion state evolved. Candidate values of the regularization factor were then evaluated using the current inversion state, and the value corresponding to the L-curve corner was selected for the subsequent update. This online Iterative-Adaptive Regularization (IAR) strategy allows the inversion to relax the prior constraint when large systematic errors remain, while increasing the effective constraint when the solution approaches a regime where additional fitting may mainly introduce oscillation or noise. The strategy is particularly useful for multi-species inversions because chemically coupled species may reduce their observation residuals at different rates, making a fixed regularization factor less reliable throughout the full iteration sequence.

S2 AOD reconstruction equations and notation definitions

Aerosol optical depth (AOD) pseudo-observations were diagnostically reconstructed from model aerosol concentrations using a simplified extinction formulation. The extinction coefficient was represented as the sum of scattering and absorption contributions:

$$\sigma_e = \sigma_{sp}(\lambda) + \sigma_{ap}(\lambda) \quad \text{Eq. S1}$$

where $\sigma_e(\lambda)$ is the extinction coefficient at wavelength λ, and $\sigma_{sp}(\lambda)$ and $\sigma_{ap}(\lambda)$ are the scattering and absorption coefficients, respectively. Column AOD was calculated by vertically integrating the layer extinction coefficient:

$$AOD_{model} = \sum_{i=1}^{N} \left(\sigma_{sp} + \sigma_{ap}\right)_i \Delta Z_i \quad \text{Eq. S2}$$

where $\mathrm{AOD}_{\mathrm{model}}$ is the reconstructed column aerosol optical depth, *i* denotes the model layer index, N is the total number of vertical layers, $\left(\sigma_{sp} + \sigma_{ap}\right)_i$ is the layer-specific extinction coefficient composed of scattering and absorption terms, and Z_i is the thickness of layer *i*.

The scattering and absorption terms were parameterized as:

$$\sigma_{sp} = (0.003)F_t(RH)\left[NH_4^+ + SO_4^{2-} + NO_3^-\right] + (0.004)[OM] + (0.001)[FS] + (0.0006)[CM] \quad \text{Eq. S3}$$

$$\sigma_{ap} = (0.01)[LAC] \quad \text{Eq. S4}$$

where σ_{sp} and σ_{ap} are the scattering and absorption coefficients, respectively; $F_t(\mathrm{RH})$ is the hygroscopic growth factor as a function of relative humidity (RH); $\left[NH_4^+\right]$, $\left[SO_4^{2-}\right]$, and $\left[NO_3^-\right]$ are the layer concentrations of ammonium, sulfate, and nitrate aerosols; [OM] is the organic matter concentration; [FS] is the fine-soil concentration; [CM] is the coarse-mass concentration; and [LAC] is the light-absorbing carbon concentration. CM denotes the coarse-

mass term used in the AOD diagnostic and should be distinguished from PMC, which is the CMAQ coarse particulate matter emission control variable. Under this formulation, AOD should be interpreted as an integrated-response constraint derived from aerosol concentrations rather than as a one-to-one inversion of a directly emitted optical quantity. Its source-space metric therefore reflects the recovery of aerosol-related CMAQ emission controls, including primary elemental carbon (PEC), primary organic carbon (POC), and coarse particulate matter (PMC).

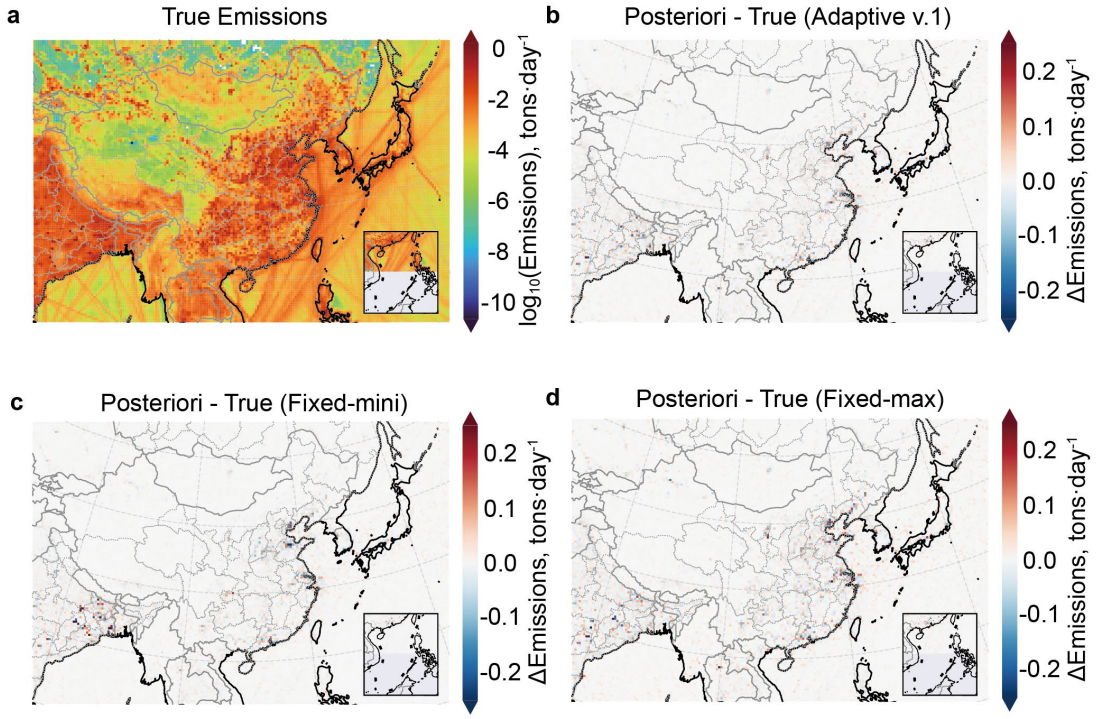

Figure S1. Spatial evaluation of posterior emission fidelity under varying regularization constraints. (a) Spatial distribution of the true SO_2 emissions (logarithmic scale). (b–d) Spatial distributions of the absolute posterior emission errors (Posterior minus True) derived from the (b) Adaptive v.1, (c) Fixed-min, and (d) Fixed-max regularization strategies.

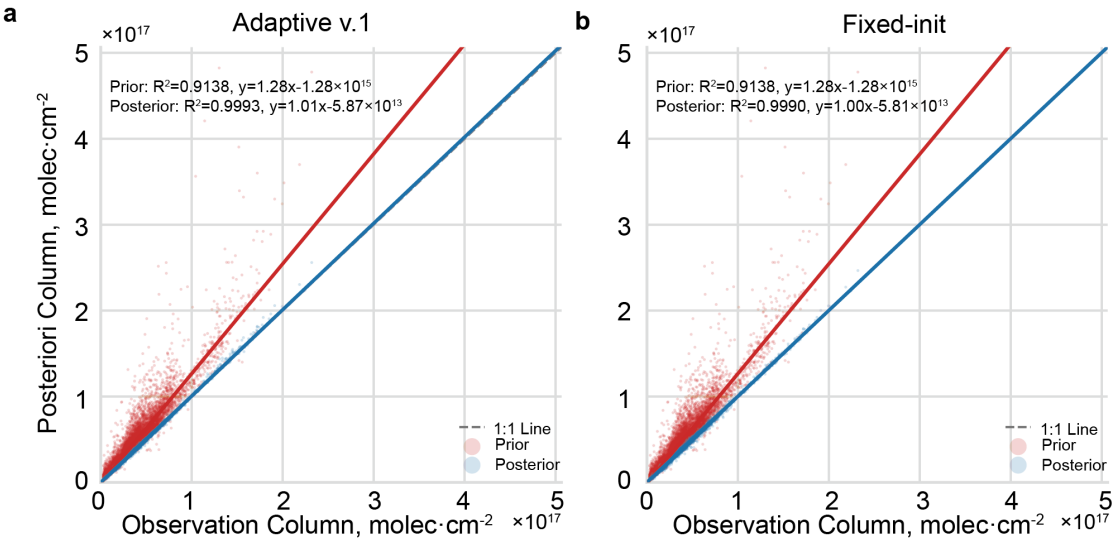

Figure S2. Scatter plots of simulated versus observed SO_2 columns. (a) Results from the IAR adaptive regularization strategy (Adaptive v.1; Case_Sens_Adaptive). (b) Results from the Fixed-init regularization strategy (Case_Sens_Fixed-init). Red points indicate the a priori state, and blue points indicate the a posteriori state. Both strategies significantly improve the correlation with observations compared to the prior, but the adaptive strategy achieves a slightly better alignment with the 1:1 line.

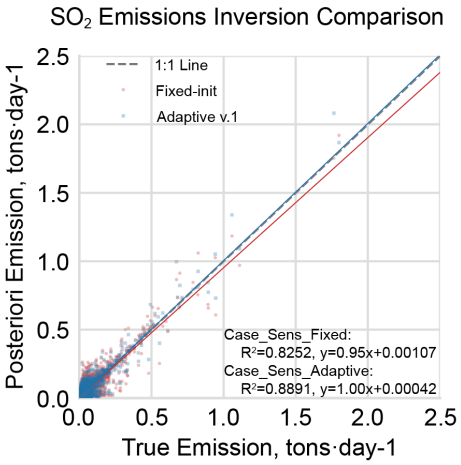

Figure S3. Comparison of the recovered posterior SO_2 emissions against the "True" emissions at the final iteration (Iteration 50). The red points and line represent the Fixed-init case (Case_Sens_Fixed-init), while the blue points and line represent the IAR adaptive case (Case_Sens_Adaptive). The dashed black line indicates the 1:1 identity line. The adaptive strategy achieves a regression slope closer to unity and a higher R^2, indicating better accuracy.

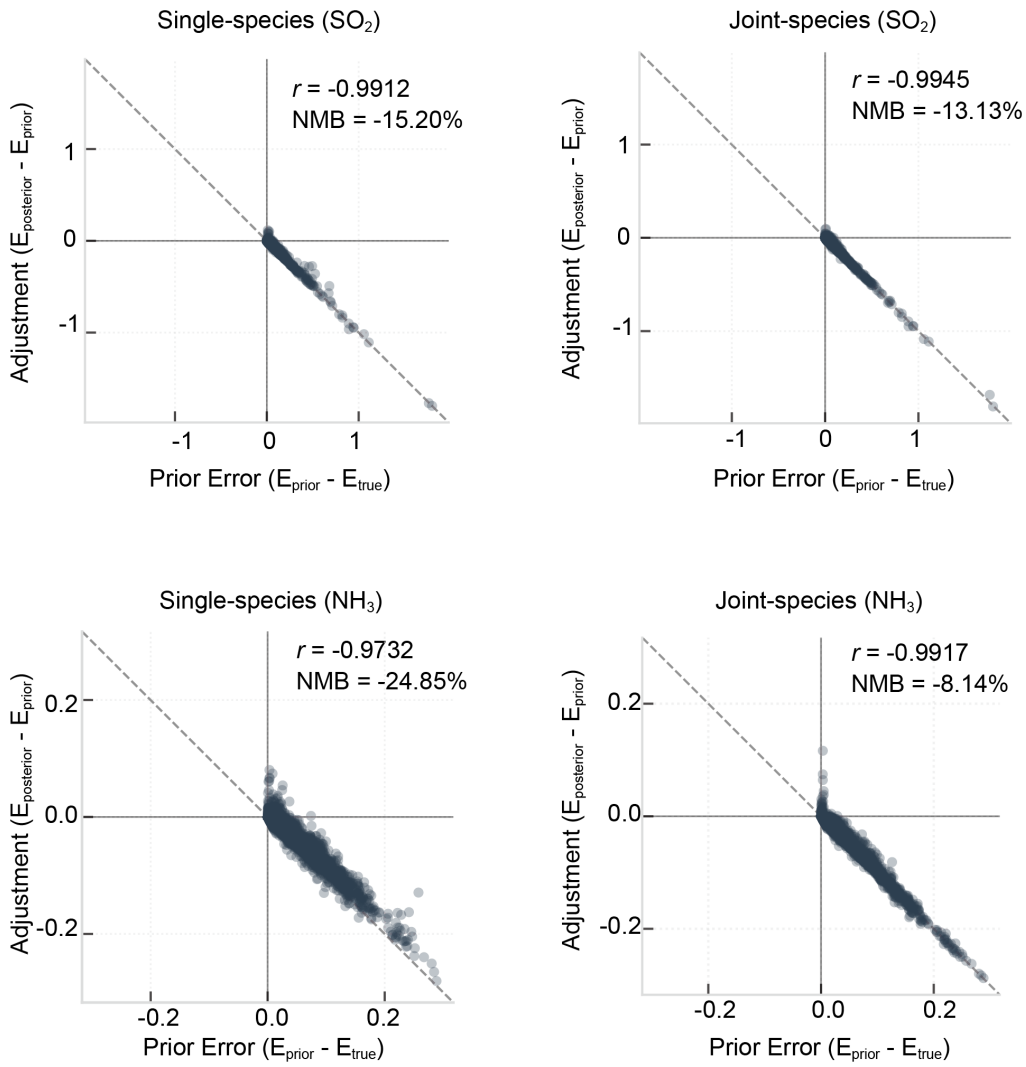

Figure S4. Evaluation of error compensation effects in single-species versus joint-species inversions. Scatter plots illustrating the posterior emission adjustment ($E_{posterior}$-E_{prior}) against the prior emission error (E_{prior}-E_{true}) for SO_2 and NH_3. The left column presents the results from the isolated single-species inversions, while the right column displays the results from the joint-species inversion. The grey dashed line denotes the ideal correction trajectory (y=−x), indicating that the inversion adjustment perfectly offsets the prior error. The solid red line

represents the linear regression of the scattered data. The noticeable deviation and lower r in the single-species NH_3 inversion reveal spurious adjustments (error compensation) caused by the unoptimized SO_2 biases. In contrast, the joint-species inversion tightly aligns with the ideal trajectory, showing that joint optimization substantially reduces cross-species error compensation.

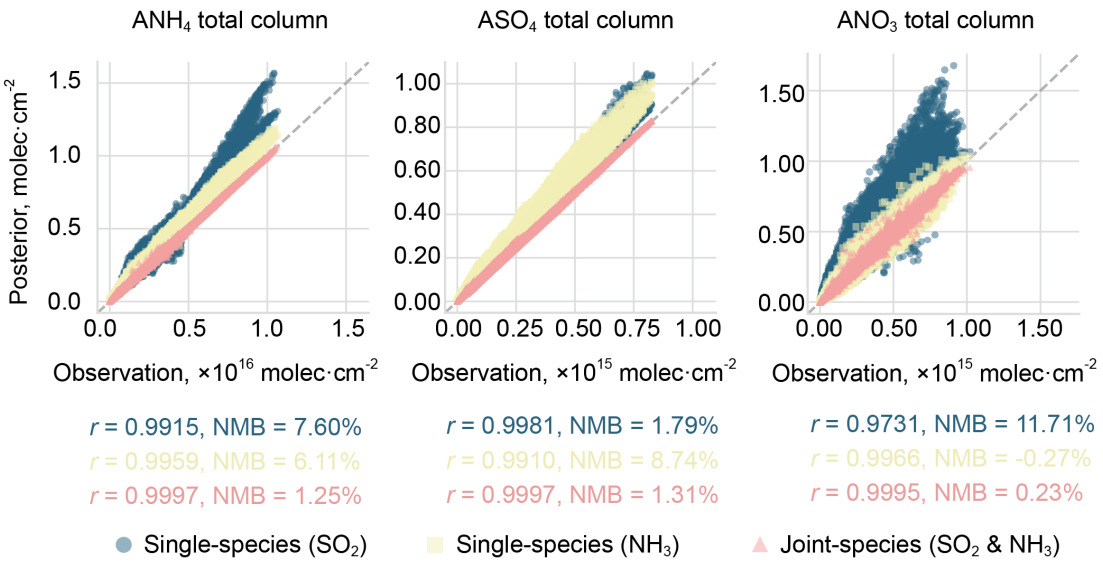

Figure S5. Validation of posterior secondary inorganic aerosol column concentrations. Scatter plots comparing the posterior simulated total columns of ammonium (ANH_4, left), sulfate (ASO_4, middle), and nitrate (ANO_3, right) against the reference ("true") columns used as pseudo-observations (units and scale factors are shown on the respective axes). The results from the single-species SO_2 inversion (circles), single-species NH_3 inversion (squares), and joint-species inversion (triangles) are evaluated. The grey dashed line represents the 1:1 reference line. The joint-species strategy consistently yields the highest correlation coefficient (r) across all three aerosol components, indicating that joint optimization better captures thermodynamic coupling within the sulfate-nitrate-ammonium (SNA) system in these experiments.

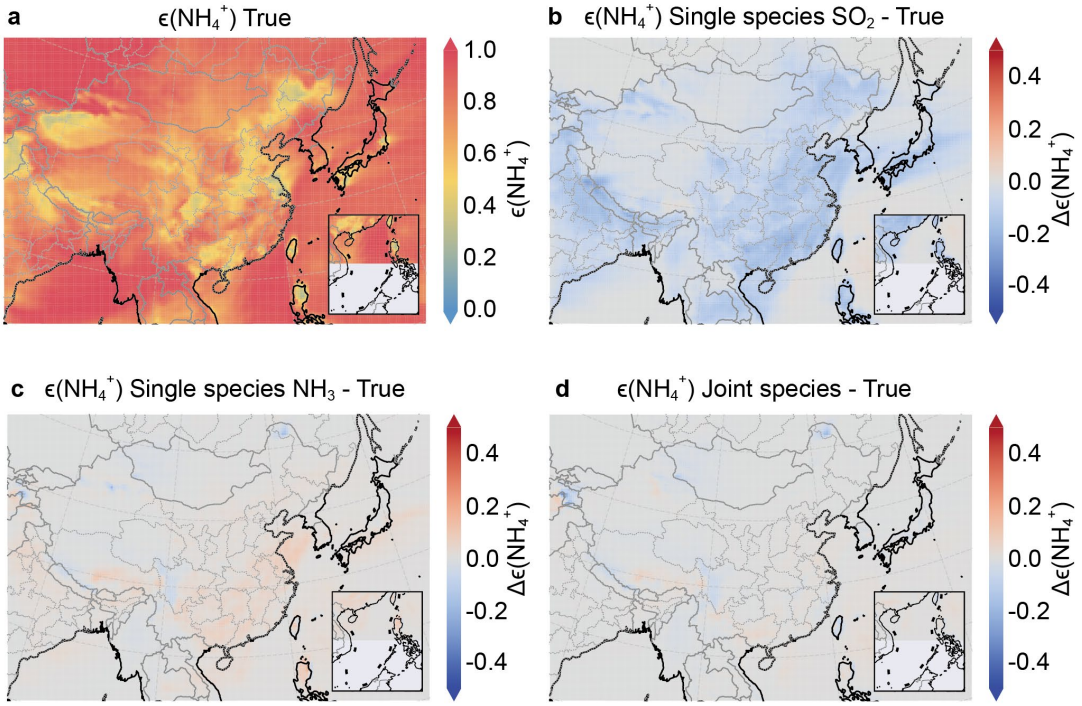

Figure S6. Spatial distribution of the ammonium partitioning coefficient and inversion-induced biases. (a) Spatial distribution of the true ammonium partitioning coefficient, defined as $\varepsilon\left(NH_4^+\right) = \frac{\left[NH_4^+\right]}{\left(\left[NH_4^+\right]+\left[NH_3\right]\right)}$, where larger values indicate a greater fraction of total ammonium in the particulate phase. (b-d) Signed differences between the posterior and true ε fields for the single-species SO_2 inversion (b), single-species NH_3 inversion (c), and joint-species inversion (d). Positive values indicate overestimation of the particulate ammonium fraction, whereas negative values indicate underestimation. The joint-species inversion reduces the magnitude of the bias relative to the single-species SO_2 inversion, although the single-species NH_3 inversion remains slightly closer to the truth under this metric.

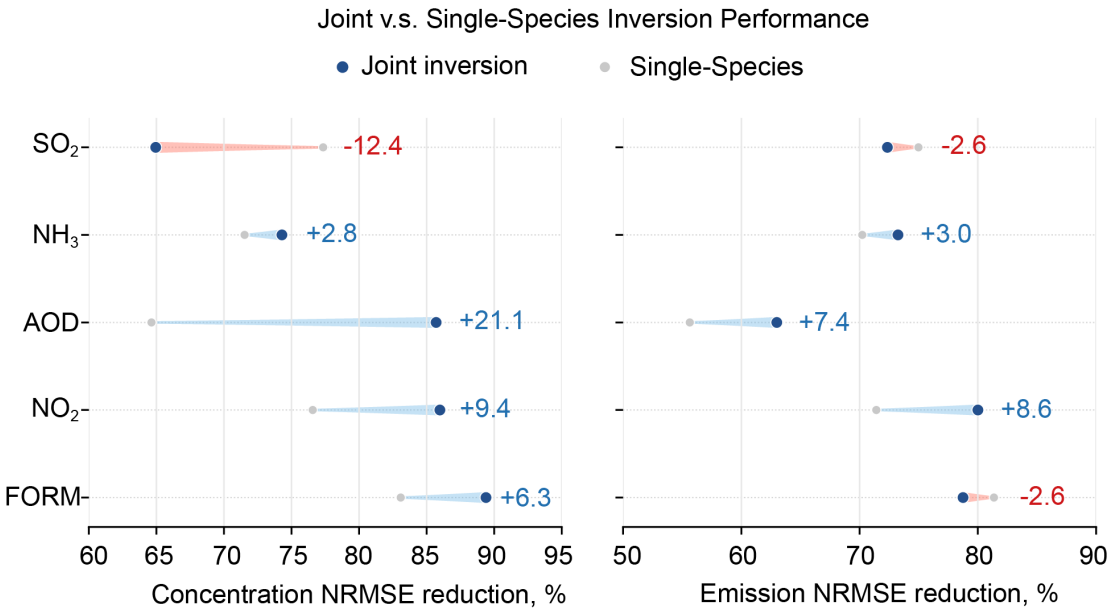

Figure S7. Joint-versus-single inversion performance under heterogeneous prior errors. The left and right panels show the prior-to-posterior reduction in concentration normalized root mean square error (NRMSE) and emission NRMSE, respectively, for sulfur dioxide (SO_2), ammonia (NH_3), aerosol optical depth (AOD), nitrogen dioxide (NO_2), and formaldehyde (FORM). Blue and gray symbols represent the joint and corresponding single-species inversions. Numbers indicate the additional reduction achieved by the joint inversion relative to the single-species inversion. Positive values indicate an advantage of the joint inversion, whereas negative values indicate better performance of the single-species inversion. Because AOD is an integrated-response constraint, its source-space metric should be interpreted as the recovery of aerosol-related emission controls rather than a one-to-one inversion of a directly emitted species.

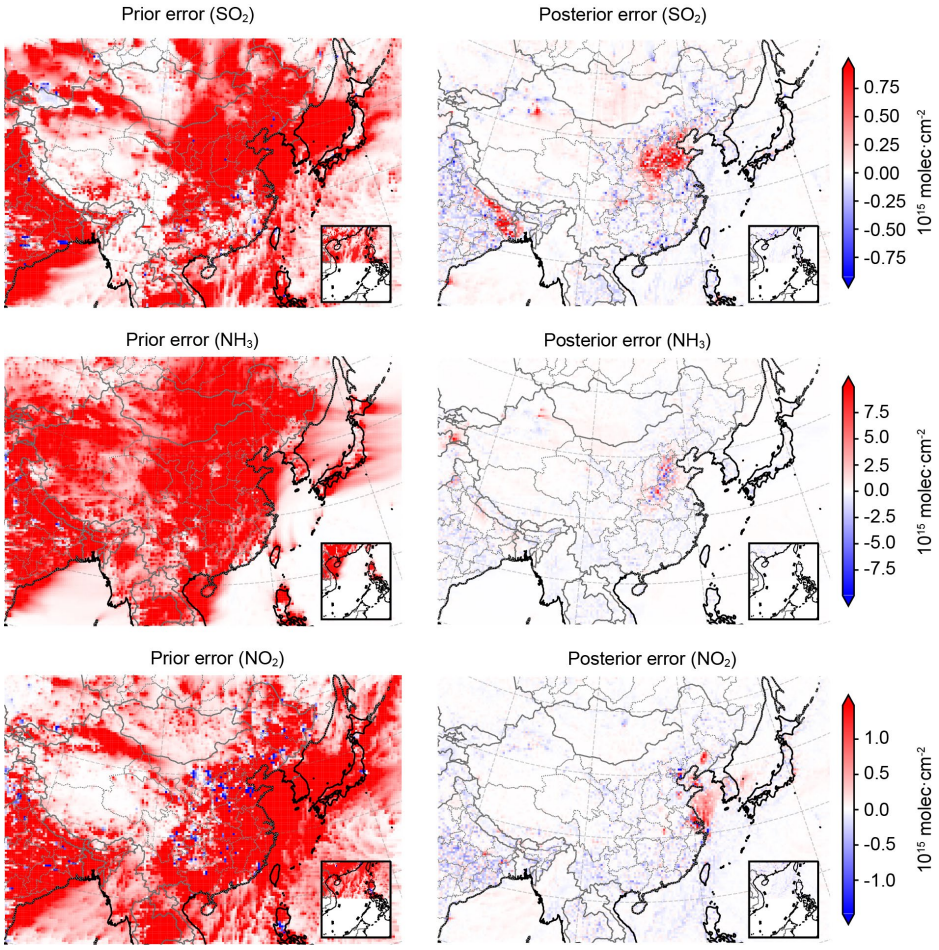

Figure S8. Spatial distribution of prior and posterior concentration errors for SO_2, NH_3, and NO_2 over the East Asian model domain. For each species, the left panel shows the prior error based on the initial joint inversion state (s0), and the right panel shows the posterior error based on the mean of the final five joint-inversion iterations (mean(s46-s50)). Errors are defined as model − truth, such that positive values indicate overestimation and negative values indicate underestimation. For gaseous species, the color scale is given in 10^{15} molecules·cm^{-2}. Boundaries and the South China Sea inset provide geographic reference; tighter symmetric scales emphasize posterior structures.

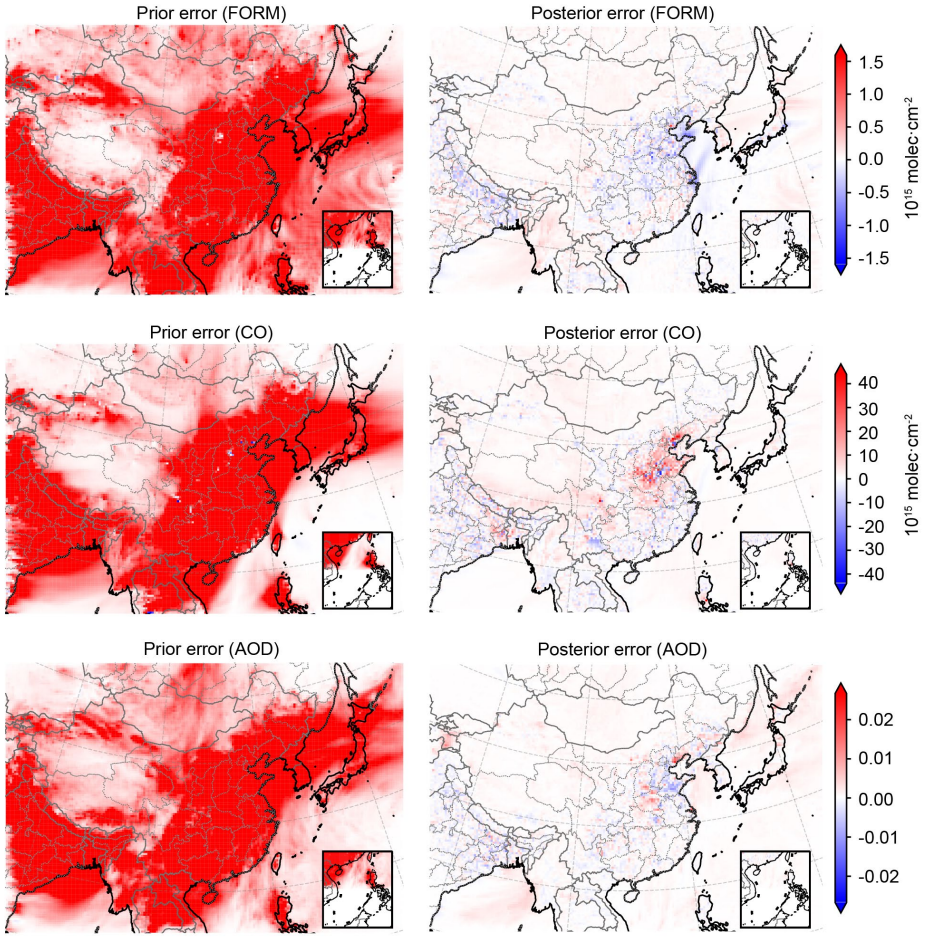

Figure S9. Spatial distribution of prior and posterior concentration errors for FORM, CO, and AOD over the East Asian model domain. For each field, the left panel shows the prior error from the initial joint inversion state (s0), and the right panel shows the posterior error from the average of the last five joint-inversion iterations (mean(s46-s50)). Errors are calculated as model − truth, with positive values indicating overestimation and negative values indicating underestimation. For FORM and CO, the color scale is expressed in 10^{15} molecules·cm^{-2}, whereas AOD is dimensionless. Boundaries and the South China Sea inset provide geographic reference; symmetric scales emphasize the remaining posterior error patterns.

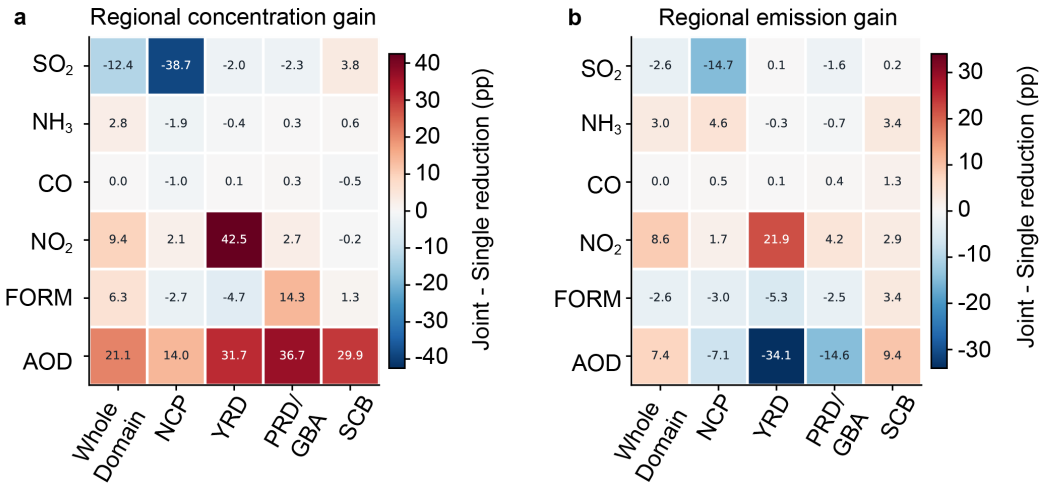

Figure S10. Regional contrast in the additional benefit of joint inversion relative to single-species inversion across the whole model domain and key subregions. (a) Extra concentration reduction, defined as the reduction in concentration NRMSE achieved by the joint inversion minus that achieved by the corresponding single-species inversion. (b) Extra emission reduction, defined analogously for emission NRMSE. Positive values indicate that the joint inversion outperforms the single-species inversion, whereas negative values indicate the opposite. Columns represent the whole domain, the North China Plain (NCP), the Yangtze River Delta (YRD), the Pearl River Delta/Greater Bay Area (PRD/GBA), and the Sichuan Basin. Rows represent the six observational constraints; for AOD, the emission-space metric refers to the associated aerosol-related emission controls. All comparisons are referenced to the common 4D-Var starting point (s4).

Table S1. Summary of experimental configurations for the Observing System Simulation Experiments (OSSEs).

Experiment group	Case ID	Prior perturbation scheme	Regularization strategy	Inversion configuration	Optimized emissions / constraints
Regularization sensitivity	Case_Sens_Fixed-init	Spatially heterogeneous	Fixed-init	Single-species inversion	SO_2
	Case_Sens_Fixed-mean	Spatially heterogeneous	Fixed-mean	Single-species inversion	SO_2
	Case_Sens_Fixed-min	Spatially heterogeneous	Fixed-min	Single-species inversion	SO_2
	Case_Sens_Fixed-max	Spatially heterogeneous	Fixed-max	Single-species inversion	SO_2
	Case_Sens_Adaptive	Spatially heterogeneous	IAR	Single-species inversion	SO_2
Idealized chemical-coupling experiment	Case_Mech_Single	Uniform scaling, 200%	IAR	Single-species inversion	SO_2-only and NH_3-only
	Case_Mech_Joint	Uniform scaling, 200%	IAR	Joint inversion	SO_2 and NH_3
Realistic heterogeneous-error experiment	Case_Real_Single	Spatially heterogeneous	IAR	Corresponding single-species inversions	SO_2, NH_3, NO_x/NO_2, CO, lumped VOCs/FORM, and aerosol/AOD-related controls
	Case_Real_Joint	Spatially heterogeneous	IAR	Multi-species joint inversion	SO_2, NH_3, NO_x/NO_2, CO, lumped VOCs/FORM, and aerosol/AOD-related controls

Note. The fixed-regularization cases used the same single-species SO_2 inversion setup but prescribed the Fixed-init, Fixed-mean, Fixed-max, and Fixed-min regularization levels. These cases correspond to the fixed-parameter strategies compared with IAR in Figure 2. In the realistic heterogeneous tests, single-species inversions were conducted as baselines for the corresponding joint inversion. FORM represents a constraint on a lumped VOCs emission control variable, whereas AOD represents an integrated-response constraint linked to aerosol-related CMAQ emission controls, including PEC, POC, and PMC. NO_2 and FORM denote the evaluated concentration constraints associated with NO_x and lumped VOCs emission controls, respectively.

Table S2. VOCs species included in the lumped VOCs control variable used for the FORM-constrained inversion.

Species	Molecular weight ($g \cdot mol^{-1}$)
Acetaldehyde (ALD2)	44.05
propionaldehyde and higher aldehydes (ALDX)	25.80
Benzene (BENZENE)	78.11
Ethene (ETH)	28.05
Ethane (ETHA)	30.07
Ethanol (ETOH)	46.07
Formaldehyde (FORM)	30.03
Internal olefin carbon bond (IOLE)	44.62
Isoprene (ISOP)	68.12
Methanol (MEOH)	32.04
Terminal olefin carbon bond (OLE)	64.39
Paraffin carbon bond (PAR)	1.00
Terpene (TERP)	160.00
Toluene and other monoalkyl aromatics (TOL)	61.09
Xylene and other polyalkyl aromatics (XYL)	106.17

Table S3. Composition of the integrated MEIC emission inventory used in this study.

Region / Sector	Description	Developer / Reference
National Baseline	MEIC v1.3 (Multi-resolution Emission Inventory for China)	Tsinghua University (Li et al., 2017; Zheng et al., 2018; Wu et al., 2024)
Yangtze River Delta (YRD)	High-resolution regional inventory	Nanjing University (Prof. Yu Zhao) (Zhou et al., 2017b; An et al., 2021)
Greater Bay Area (GBA)	High-resolution regional inventory for Guangdong-Hong Kong-Macau	Jinan University (Prof. Junyu Zheng) (Zheng et al., 2009; Huang et al., 2021; Sha et al., 2021)
Ammonia (NH_3)	National high-resolution ammonia emission inventory	Peking University (Prof. Yu Song) (Huang et al., 2012b; Kang et al., 2016)
Biomass Burning	National open biomass burning inventory	Peking University (Prof. Yu Song) (Song et al., 2009; Huang et al., 2012a; Liu et al., 2015; Yin et al., 2019)
Straw Burning	National straw open burning inventory	Beijing University of Technology (Prof. Ying Zhou) (Zhou et al., 2017a)
Shipping	East Asia shipping emission inventory	Tsinghua University (Prof. Huan Liu) (Liu et al., 2016; Liu et al., 2019)

References

An, J., Huang, Y., Huang, C., Wang, X., Yan, R., Wang, Q., Wang, H., Jing, S., Zhang, Y., Liu, Y., Chen, Y., Xu, C., Qiao, L., Zhou, M., Zhu, S., Hu, Q., Lu, J., and Chen, C.: Emission Inventory of Air Pollutants and Chemical Speciation for Specific Anthropogenic Sources Based on Local Measurements in the Yangtze River Delta Region, China, Atmos. Chem. Phys., 21, 2003–2025, https://doi.org/10.5194/acp-21-2003-2021, 2021.

Huang, X., Li, M., Li, J., and Song, Y.: A High-Resolution Emission Inventory of Crop Burning in Fields in China Based on MODIS Thermal Anomalies/Fire Products, Atmos. Environ., 50, 9–15, https://doi.org/10.1016/j.atmosenv.2012.01.017, 2012a.

Huang, X., Song, Y., Li, M., Li, J., Huo, Q., Cai, X., Zhu, T., Hu, M., and Zhang, H.: A High-Resolution Ammonia Emission Inventory in China, Global Biogeochem. Cy., 26, GB1030, https://doi.org/10.1029/2011GB004161, 2012b.

Huang, Z., Zhong, Z., Sha, Q., Xu, Y., Zhang, Z., Wu, L., Wang, Y., Zhang, L., Cui, X., Tang, M., Shi, B., Zheng, C., Li, Z., Hu, M., Bi, L., Zheng, J., and Yan, M.: An Updated Model-Ready Emission Inventory for Guangdong Province by Incorporating Big Data and Mapping onto Multiple Chemical Mechanisms, Sci. Total Environ., 769, 144535, https://doi.org/10.1016/j.scitotenv.2020.144535, 2021.

Kang, Y., Liu, M., Song, Y., Huang, X., Yao, H., Cai, X., Zhang, H., Kang, L., Liu, X., Yan, X., He, H., Zhang, Q., Shao, M., and Zhu, T.: High-Resolution Ammonia Emissions Inventories in China from 1980 to 2012, Atmos. Chem. Phys., 16, 2043–2058, https://doi.org/10.5194/acp-16-2043-2016, 2016.

Li, M., Liu, H., Geng, G., Hong, C., Liu, F., Song, Y., Tong, D., Zheng, B., Cui, H., Man, H., Zhang, Q., and He, K.: Anthropogenic Emission Inventories in China: A Review, Natl. Sci. Rev., 4, 834–866, https://doi.org/10.1093/nsr/nwx150, 2017.

Liu, H., Fu, M., Jin, X., Shang, Y., Shindell, D., Faluvegi, G., Shindell, C., and He, K.: Health and Climate Impacts of Ocean-Going Vessels in East Asia, Nat. Clim. Change, 6, 1037–1041, https://doi.org/10.1038/nclimate3083, 2016.

Liu, H., Meng, Z.-H., Lv, Z.-F., Wang, X.-T., Deng, F.-Y., Liu, Y., Zhang, Y.-N., Shi, M.-S., Zhang, Q., and He, K.-B.: Emissions and Health Impacts from Global Shipping Embodied in US-China Bilateral Trade, Nat. Sustain., 2, 1027–1033, https://doi.org/10.1038/s41893-019-0414-z, 2019.

Liu, M., Song, Y., Yao, H., Kang, Y., Li, M., Huang, X., and Hu, M.: Estimating Emissions from Agricultural Fires in the North China Plain Based on MODIS Fire Radiative Power, Atmos. Environ., 112, 326–334, https://doi.org/10.1016/j.atmosenv.2015.04.058, 2015.

Sha, Q., Zhu, M., Huang, H., Wang, Y., Huang, Z., Zhang, X., Tang, M., Lu, M., Chen, C., Shi, B., Chen, Z., Wu, L., Zhong, Z., Li, C., Xu, Y., Yu, F., Jia, G., Liao, S., Cui, X., Liu, J., and Zheng, J.: A Newly Integrated Dataset of Volatile Organic Compounds (VOCs) Source Profiles and Implications for the Future Development of VOCs Profiles in China, Sci. Total Environ., 793, 148348, https://doi.org/10.1016/j.scitotenv.2021.148348, 2021.

Song, Y., Liu, B., Miao, W., Chang, D., and Zhang, Y.: Spatiotemporal Variation in Nonagricultural Open Fire Emissions in China from 2000 to 2007, Global Biogeochem. Cy., 23, GB2008, https://doi.org/10.1029/2008GB003344, 2009.

Wu, N., Geng, G., Xu, R., Liu, S., Liu, X., Shi, Q., Zhou, Y., Zhao, Y., Liu, H., Song, Y., Zheng, J., Zhang, Q., and He, K.: Development of a High-Resolution Integrated Emission Inventory of Air Pollutants for China, Earth Syst. Sci. Data, 16, 2893–2915, https://doi.org/10.5194/essd-16-2893-2024, 2024.

Yin, L., Du, P., Zhang, M., Liu, M., Xu, T., and Song, Y.: Estimation of Emissions from Biomass Burning in China (2003-2017) Based on MODIS Fire Radiative Energy Data, Biogeosciences, 16, 1629–1640, https://doi.org/10.5194/bg-16-1629-2019, 2019.

Zheng, B., Tong, D., Li, M., Liu, F., Hong, C., Geng, G., Li, H., Li, X., Peng, L., Qi, J., Yan, L., Zhang, Y., Zhao, H., Zheng, Y., He, K., and Zhang, Q.: Trends in China's Anthropogenic Emissions since 2010 as the Consequence of Clean Air Actions, Atmos. Chem. Phys., 18, 14095–14111, https://doi.org/10.5194/acp-18-14095-2018, 2018.

Zheng, J., Zhang, L., Che, W., Zheng, Z., and Yin, S.: A Highly Resolved Temporal and Spatial Air Pollutant Emission Inventory for the Pearl River Delta Region, China and Its Uncertainty Assessment, Atmos. Environ., 43, 5112–5122, https://doi.org/10.1016/j.atmosenv.2009.04.060, 2009.

Zhou, Y., Xing, X., Lang, J., Chen, D., Cheng, S., Wei, L., Wei, X., and Liu, C.: A Comprehensive Biomass Burning Emission Inventory with High Spatial and Temporal Resolution in China, Atmos. Chem. Phys., 17, 2839–2864, https://doi.org/10.5194/acp-17-2839-2017, 2017a.

Zhou, Y., Zhao, Y., Mao, P., Zhang, Q., Zhang, J., Qiu, L., and Yang, Y.: Development of a High-Resolution Emission Inventory and Its Evaluation and Application through Air Quality Modeling for Jiangsu Province, China, Atmos. Chem. Phys., 17, 211–233, https://doi.org/10.5194/acp-17-211-2017, 2017b.